Efficient Homography-based Tracking and 3-D Reconstruction for Single Viewpoint Sensors

Christopher Mei, Selim Benhimane, Ezio Malis, *Member, IEEE*, and Patrick Rives, *Member, IEEE*

***Abstract*— This paper addresses the problem of motion estimation and 3-D reconstruction through visual tracking with a single viewpoint sensor and in particular how to generalise tracking to calibrated omnidirectional cameras. We analyse different minimisation approaches for the intensity-based cost function (sum-of-squared differences). In particular, we propose novel variants of the efficient second-order minimisation (ESM) with better computational complexities and compare these algorithms with the inverse composition (IC) and the hyperplane approximation (HA). Issues regarding the use of the IC and HA for 3-D tracking are discussed. We show that even though an iteration of ESM is more computationally expensive than an iteration of IC, the faster convergence rate makes it globally faster. The tracking algorithm was validated using an omnidirectional sensor mounted on a mobile robot.**

***Index Terms*— visual tracking, structure from motion, omnidirectional vision**

I. Introduction

WIDE field of view cameras are becoming increasingly popular in mobile robotics as they offer advantages in tasks such as motion estimation, autonomous navigation and localisation [1]. Recent research using omnidirectional cameras has been focused on ego-motion estimation [2], [3] and visual servoing [4], [5]. Visual tracking, which is a fundamental step for various computer vision and robotic applications, has seen very few articles. The advantages of direct visual tracking in terms of precision have been shown for perspective cameras [6] and stereo pairs [7] which motivates the extension of tracking to omnidirectional cameras.

The tracking approach presented in this work minimizes a dissimilarity measure and more specifically a sum-of-squared-differences (SSD) between a reference template and the current image taken with a large field of view sensor. This leads to a non-linear optimization problem that can be solved for small displacements (the type of movement that would be expected in a scene at video rate). The advantage of SSD tracking is precision (all the information is being used leading to sub- pixel accuracy) and speed ($\sim$ 100Hz). This is why these techniques are particularly well adapted to robotic tasks such as visual servoing and as an input to simultaneous localisation and mapping (SLAM) algorithms. The downside is the need for a strong overlap between the reprojected and the real object for the algorithm to converge.

The apparent difficulty of tracking with omnidirectional sensors comes from the non-linear projection model resulting in changes of shape in the image that makes the direct use of methods such as KLT [8], [9] nearly impossible. Parametric models [10], [11], [12] such as the homography-based approach presented in this article are well adapted to this problem. Previous related work using homography-based tracking for perspective cameras include [13], [14] which extend the work proposed by Hager [10]. Homographies have also been used for visual servoing with central catadioptric cameras [5], [15] and share with our approach the notion of homographies for points belonging to the sphere of the unified projection model. We assume in this work that the camera has been calibrated. The single viewpoint property means it would be possible to track in an unwarped perspective view. This is however undesirable for the following reasons:

1) it introduces a discontinuity in the Jacobian (at least two planes are needed to represent the 360 deg field of view),
2) the non-uniform resolution is not taken into account and
3) the approach is inefficient (in terms of speed and memory usage).

To our knowledge, this is the only work on SSD tracking for omnidirectional sensors. The closest work is that of Barreto *et al* [4]. The authors propose a method for tracking omnidirectional lines using a contour-to-point tracker to avoid the problem of quadric-based catadioptric line fitting. In [16] and [17], the authors estimate the position of a perspective camera assuming known plane positions. In our work, the plane normals and distances are estimated. Compared to methods such as [18] and [19], we proceed in an iterative minimisation to achieve better accuracy and more reliable convergence, as will be discussed in Section IV-B. This article is also related to [17] where the authors introduce the ESM algorithm for 2-D homography-based tracking. In this article, we propose novel variants to the ESM and show how to apply the algorithm to jointly estimate the pose and plane positions (instead of separate tracking) in a more general omnidirectional framework.

In this paper, we will not discuss the important aspects of a complete visual SLAM solution such as automatic plane initialisation ([20], [21]) and re-localisation ([22], [23]) that are required in a complete visual SLAM solution. The focus of this article is on the tracking aspect, how to extend tracking

Manuscript received July 30, 2007; revised September 21, 2008. Part of this work was presented at the IEEE/RSJ International Conference on Intelligent Robot Systems, Beijing, China, October 2006 and at the British Machine Vision Conference, Edinburgh, UK, September 2006.

C. Mei is with the Robotics Research Group, Department of Engineering Science, University of Oxford, OX1 3PJ, UK. Email: christopher.mei@eng.ox.ac.uk

S. Benhimane is with the Technische Universität München, 85748 Garching b. München, Germany. Email: selim.benhimane@cs.tum.edu

E. Malis and P. Rives are with with the Institut National de Recherche en Informatique et en Automatique, 06902 Sophia-Antipolis Cedex, France. {ezio.malis,patrick.rives}@sophia.inria.fr

to omnidirectional cameras, its relation to motion estimation and efficient minimisation approaches.

The article will be organised in the following way. We will start by introducing the concept of spherical perspective projection which is adapted to large field of view sensors. We will then detail the geometric transformation considered in this work: planar homographies. Homographies have the advantage of encompassing all perspective planar deformations and thus enable to track over long sequences and avoid drift. Changes in illumination will not be considered for clarity. Affine photometric models can be introduced without changing the underlying results using for example [10]. More advanced models, taking into account for example specularities, are still object of research and not the topic of this article. Section III will discuss the problem of minimisation, how to obtain second-order convergence and apply it to single and multi plane tracking with single viewpoint sensors (thus obtaining the pose of the camera and the positions of the 3-D planes). Simulated and real data experiments validate the proposed algorithms and confirm the advantages compared to standard algorithms such as the inverse compositional [24] or hyperplane approximation [25]. The algorithm was evaluated on the motion estimation of a mobile robot and the results are compared to the precise odometry considered as ground truth.

II. Projection models and geometric transformations

Single viewpoint omnidirectional sensors are perspective sensors so all standard properties such as planar homographies stay valid as we will illustrate in this section. The standard projection model needs to be adapted however to allow points to be "behind" the camera, this will be done through the use of the spherical perspective projection.

A. Perspective projection models

1) Planar perspective projection: The standard projection model used for perspective cameras can be summarised in the following steps (FIG. 1):

1) a 3-D point $(\boldsymbol{\mathcal{P}})_{\mathcal{F}_c} = (X, Y, Z)$ in the camera reference frame is projected to the *normalised* plane π_m:
$$(\boldsymbol{\mathcal{P}})_{\mathcal{F}_c} \longrightarrow \mathbf{m} = (x, y, 1) = (\frac{X}{Z}, \frac{Y}{Z}, 1)$$
2) with $\mathbf{K}$ the matrix of intrinsic parameters ([26]) the projection of $\mathbf{m}$ in homogeneous coordinates to the image plane π_p is obtained linearly by:
$$\mathbf{p} = (u, v, 1) = \mathbf{K}\mathbf{m}$$

For a field of view greater than 180 deg., this model is not adapted. With a unique plane, there is an ambiguity between the front and the back of the camera which makes metric reconstruction impossible.

2) Spherical perspective projection: Instead of projecting the points to the unit plane π_m, we can project the points to the unit sphere $\mathbb{S}^2 = \{\boldsymbol{\mathcal{S}} \in \mathbb{R}^3 | \|\boldsymbol{\mathcal{S}}\| = 1\}$ (see Fig. 2). We will note $\boldsymbol{\mathcal{S}}$ the points on $\mathbb{S}^2$. The cheirality constraint[1] can

[1]constraint that the scene points are in front of the camera

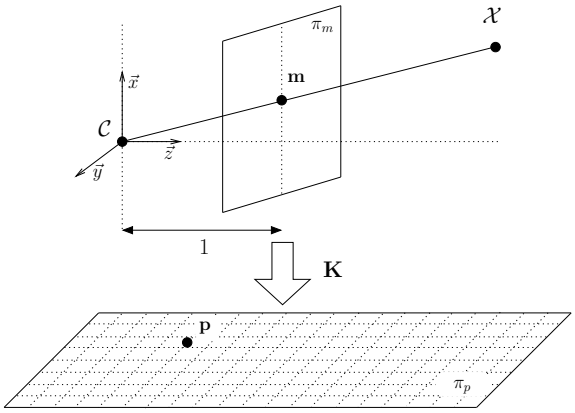

Fig. 1. Planar perspective projection

be expressed in the following way: the scale factor λ relating points on the sphere to the 3-D points must be positive:

$$\exists \boldsymbol{\mathcal{S}} \in \mathbb{S}^2 \implies \exists \lambda > 0 | \boldsymbol{\mathcal{P}} = \lambda \boldsymbol{\mathcal{S}} \tag{1}$$

From the unit sphere, we can then apply a projection function noted $\Pi : \Upsilon \subsetneq \mathbb{S}^2 \rightarrow \Omega \subset \mathbb{R}^2$ that depends on the intrinsic parameters of the sensor.

An important observation is that for single viewpoint sensor, Π is a bijective function defined over a subset of $\mathbb{S}^2$ ($\mathbb{S}^2$ and $\mathbb{R}^2$ do not share the same topology). Π^{-1} will relate points from the image plane to their projective rays (lifting).

In this work, the projection model used for the omnidirectional sensors is the model proposed in [27] based on the work by Geyer [28] and Barreto [29]. It has the advantage of being valid for a large class of sensors: central catadioptric sensors, fish-eye lenses and spherical mirrors.

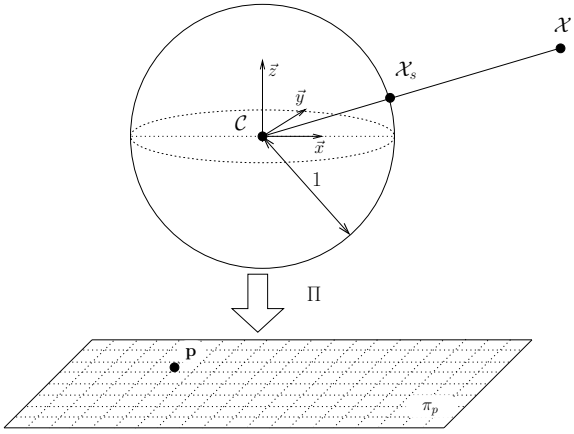

Fig. 2. Spherical perspective projection

B. Homographies for the spherical perspective projection model

Let $\mathbf{R} \in \mathbb{SO}(3)$ be the rotation of the camera and $\mathbf{t} \in \mathbb{R}^3$ its translation. The standard planar homography matrix $\mathbf{H}$ is defined up to a scale factor:

$$\mathbf{H} \sim \mathbf{R} + \mathbf{t}\mathbf{n}_d^{*\top} \tag{2}$$

where $\mathbf{n}_d^* = \mathbf{n}^*/d^*$ is the ratio between the normal vector to the plane $\mathbf{n}^*$ (a unit vector) and the distance d^* of the plane to the origin of the reference frame. In the following sections, we will call $\mathbf{n}_d^*$ the plane normal by "abuse of language". The transformation induced by a homography stays valid for all single viewpoint sensors. Figure 3 illustrates the transformation induced by a planar homography using the spherical perspective projection model. The points $\boldsymbol{\mathcal{S}}^*$ and $\boldsymbol{\mathcal{S}}$ are related by:

$$\exists(\rho,\rho^*)\in\mathbb{R}^2,\ \ \boldsymbol{\mathcal{P}}=\rho\boldsymbol{\mathcal{S}}=\rho^*\mathbf{H}\boldsymbol{\mathcal{S}}^* \tag{3}$$

A homography is defined up to a scale factor. In order to fix the scale, we choose $\det(\mathbf{H})=1$, i.e. $\mathbf{H}\in\mathbb{SL}(3)$ (the Special Linear group of dimension 3). Indeed $\det(\mathbf{H})=0$ happens only if the observed plane passes through the optical center of the camera and is then no longer visible.

From a homography, it is possible to extract the transformation and plane normal. However two solutions are obtained which explains why we have to distinguish the tracking of a single plane (through a unique homography) and tracking multiple planes.

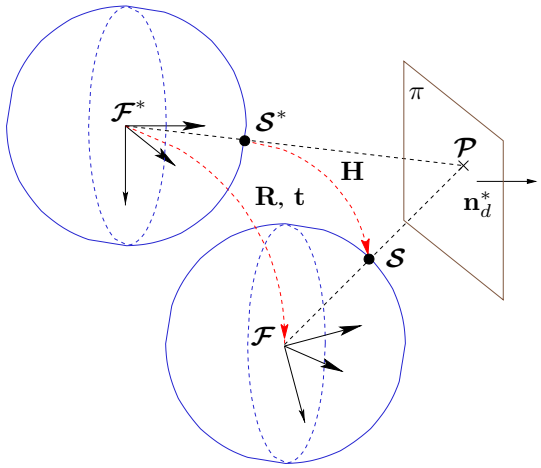

Fig. 3. Planar homography for the spherical perspective projection

C. Warping

We will call *warping*, noted $\mathbf{w}:\mathbb{SL}(3)\times\mathbb{S}^2\longrightarrow\mathbb{S}^2$, a coordinate transformation induced by a homography $\mathbf{H}\in\mathbb{SL}(3)$ between points on a sphere: This group transformation has the following properties:

- $\mathbf{w}<\mathbf{I}><\boldsymbol{\mathcal{S}}>$ is the identity map: $\forall\boldsymbol{\mathcal{S}}\in\mathbb{S}^2, \mathbf{w}<\mathbf{I}><\boldsymbol{\mathcal{S}}>=\boldsymbol{\mathcal{S}}$
- the composition of two actions corresponds to the action of the composition:

$$\forall\boldsymbol{\mathcal{S}}\in\mathbb{S}^2,\ \forall(\mathbf{H}_1,\mathbf{H}_2)\in\ \mathbb{SL}(3)^2,$$
$$\mathbf{w}<\mathbf{H}_1><\mathbf{w}<\mathbf{H}_2><\boldsymbol{\mathcal{S}}>>=\mathbf{w}<\mathbf{H}_1\mathbf{H}_2><\boldsymbol{\mathcal{S}}>$$

Practically, warping consists in finding the intensity of the transformation of an image point in a new view. Due to discretisation, we will have to calculate an *approximate* intensity in the new position. For omnidirectional sensors, the intensity in a given point depends on the solid angle formed by a pixel and the interpolation should take into account the geodesic distance on the unit sphere. However what is important is the relative distance that will only change slightly due to distortion as the calculation is *local*. In this work, the image warpings were done with a bilinear transformation taken in the image.

III. Homography-based visual tracking

A. Incremental tracking and motion estimation

Let $\mathcal{I}^*$ be the reference image. We will call reference template noted $\mathcal{R}$ a region $\mathcal{I}^*$ corresponding to the projection of a planar region of the scene. Let $\mathcal{I}_t, t=1..T$ be a sequence of images. Tracking corresponds to finding the projection of the pixels $\mathbf{p}\in\mathcal{R}$ in the sequence of images.

The estimation of a generic transformation $\mathcal{T}$ in a image sequence is done incrementally, the previous calculated values being used as initial estimates for the following transformations, $\widehat{\mathcal{T}}_{0(i+1)}=\overline{\mathcal{T}}_{0i}$. If convergence is obtained at each step, we obtain the optimal transformation $\overline{\mathcal{T}}$ between the first and the last view without drift as illustrated in Fig. 4. $\mathcal{T}(\mathbf{x})$ corresponds to the increment that is estimated at each step.

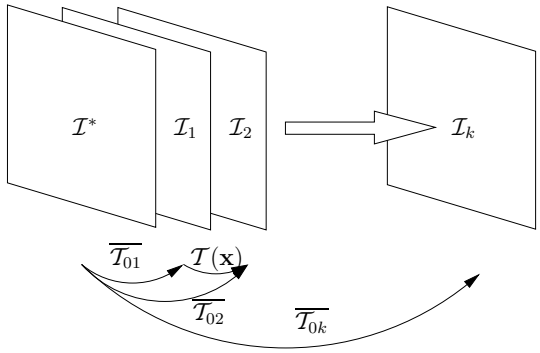

Fig. 4. Incremental calculation of the transformation

The projection of a point belonging to a planar region follows a planar homography noted $\mathbf{H}$. Thus if the only transformation that has occurred to the template is geometric (as is assumed in this article), tracking at time t will correspond to finding the optimal homography $\overline{\mathbf{H}}$ such that:

$$\forall\mathbf{p}\in\mathcal{R},\ \ \mathcal{I}_t(\overline{\mathcal{T}}_{\overline{\mathbf{H}}}(\mathbf{p}^*))=\mathcal{I}^*(\mathbf{p}^*) \tag{4}$$

In the case of multiple planes, we can either track the planes individually or impose the same camera motion as described in Section III-D. We will see that the latter choice leads to more robust motion estimates.

Finding the optimal transformation can be written as an optimisation problem over the difference in intensities. If the L_2 norm is chosen the approach is called sum-of-squared difference (SSD) tracking and the minimisation is written:

$$\overline{\mathcal{T}}_t=\text{argmin}_{\mathcal{T}_i}\frac{1}{2}\sum_{\mathbf{p}^*\in\mathcal{R}}\|\mathcal{I}_t(\mathcal{T}_i(\mathbf{p}^*))-\mathcal{I}^*(\mathbf{p}^*)\|^2 \tag{5}$$

B. Efficient second-order minimisation

SSD tracking generally relies on iterative methods to minimise the cost function. First-order methods or methods with final super-linear convergence (eg. Levenberg-Marquardt or Dog Leg) are generally employed as calculating the Hessian to obtain full quadratic convergence is computationally expensive.

In fact, through the Lie algebra parameterisation, we can obtain second-order convergence with a computational cost of the same order as a first-order method, this technique was dubbed efficient second-order minimisation (ESM) [30], [14]. For completeness, we will derive the main steps.

Consider the general least-squares minimisation problem:

$$F(\mathbf{x}) = \frac{1}{2}\sum_{i=1}^{n}(f_i(\mathbf{x}))^2 = \frac{1}{2}\|\mathbf{f}(\mathbf{x})\|^2 \tag{6}$$

The necessary condition for finding a local or the global minimum of the cost function is that there exists a stationary point $\mathbf{x}_0$ such that: $[\nabla_{\mathbf{x}} F]_{\mathbf{x}=\mathbf{x}_0} = \mathbf{0}$ where $\nabla_{\mathbf{x}}$ is the gradient operator with respect to $\mathbf{x}$. If this equation is non-linear, a closed-form solution is generally difficult to obtain.

A second-order Taylor series of $\mathbf{f}$ about $\mathbf{x} = \mathbf{0}$ gives:

$$\mathbf{f}(\mathbf{x}) = \mathbf{f}(\mathbf{0}) + \mathbf{J}(\mathbf{0})\,\mathbf{x} + \frac{1}{2}\mathbf{M}(\mathbf{0},\mathbf{x})\mathbf{x} + \mathcal{R}(\|\mathbf{x}\|^3) \tag{7}$$

where $\mathbf{J}(\mathbf{0}) = [\nabla_{\mathbf{x}}\mathbf{f}]_{\mathbf{x}=\mathbf{0}}$, $\mathbf{M}(\mathbf{z},\mathbf{x}) = [\nabla_{\mathbf{x}}\mathbf{J}]_{\mathbf{x}=\mathbf{z}}\mathbf{x}$ and $\mathcal{R}(\|\mathbf{x}\|^3)$ is the third-order reminder. Similarly, we can write the Taylor series of the Jacobian $\mathbf{J}$ about $\mathbf{x} = \mathbf{0}$:

$$\mathbf{J}(\mathbf{x}) = \mathbf{J}(\mathbf{0}) + \mathbf{M}(\mathbf{0},\mathbf{x}) + \mathcal{R}(\|\mathbf{x}\|^2) \tag{8}$$

Plugging (8) in (7) leads to:

$$\mathbf{f}(\mathbf{x}) = \mathbf{f}(\mathbf{0}) + \frac{1}{2}(\mathbf{J}(\mathbf{0}) + \mathbf{J}(\mathbf{x}))\,\mathbf{x} + \mathcal{R}(\|\mathbf{x}\|^3) \tag{9}$$

As $\mathbf{x}_0 \approx \mathbf{0}$, a second-order approximation of $\mathbf{f}$ in $\mathbf{x}_0$ is:

$$\mathbf{f}(\mathbf{x}_0) \approx \mathbf{f}(\mathbf{0}) + \frac{1}{2}(\mathbf{J}(\mathbf{0}) + \mathbf{J}(\mathbf{x}_0))\,\mathbf{x}_0 \tag{10}$$

Under certain conditions, that we will detail in the following sections, $\mathbf{J}(\mathbf{x}_0)\mathbf{x}_0$ can be calculated without knowing the value of $\mathbf{x}_0$. This is the basis of the ESM algorithm.

Let $\mathbf{J}(\mathbf{x}_0)\mathbf{x}_0 = \mathbf{J}'\mathbf{x}_0$, at the solution, $\mathbf{f}(\mathbf{x}_0) = 0$, so our second-order least-square minimiser is the solution to (with $^+$ the pseudo-inverse):

$$\mathbf{x}_0 = -\left(\frac{\mathbf{J}(\mathbf{0}) + \mathbf{J}'}{2}\right)^{+}\mathbf{f}(\mathbf{0}) \tag{11}$$

For comparison, the first-order minimisers for the *forward compositional* (current Jacobian) [10] and the *inverse compositional* (reference Jacobian) [24] methods are respectively:

$$\mathbf{x}_0 = -\mathbf{J}(\mathbf{0})^{+}\mathbf{f}(\mathbf{0}), \quad \mathbf{x}_0 = -\mathbf{J}'^{+}\mathbf{f}(\mathbf{0}) \tag{12}$$

An alternative formulation proposed by Jurie and Dhome [25], *hyperplane approximation*, consists in finding a matrix $\mathbf{J}^{\oplus}$ that plays the same role as the pseudo-inverse but is obtained by learning the linear relationship between the incremental motion $\mathbf{x}_0$ and $\mathbf{f}(\mathbf{0})$.

C. Tracking a single plane

Consider the following diagram, illustrated by Fig. 3:

$$\mathbf{p}^* \xrightarrow{\Pi^{-1}} \boldsymbol{\mathcal{S}}^* \xrightarrow{\mathbf{w}<\mathbf{H}><.>} \boldsymbol{\mathcal{S}} \xrightarrow{\Pi} \mathbf{p} \tag{13}$$

To track the template in the current image $\mathcal{I}$ is to find the transformation $\overline{\mathbf{H}} \in \mathbb{SL}(3)$ that warps the lifting of that region to the lifting of the reference template of $\mathcal{I}^*$, i.e. find $\overline{\mathbf{H}}$ with:

$$\forall i,\ \mathcal{I}\left(\Pi\left(\mathbf{w}<\overline{\mathbf{H}}><\boldsymbol{\mathcal{S}}_i^*>\right)\right) = \mathcal{I}^*(\mathbf{p}_i^*) \tag{14}$$

Knowing an approximation $\widehat{\mathbf{H}}$ of the transformation $\overline{\mathbf{H}}$, the problem is to find the incremental transformation $\mathbf{H}(\mathbf{x})$ that minimizes the SSD:

$$\begin{cases} F(\mathbf{x}) = \frac{1}{2}\sum_{i=1}^{q}\|\mathbf{f}_i\|^2 \\ \mathbf{f}_i = \mathcal{I}\left(\Pi\left(\mathbf{w}<\widehat{\mathbf{H}}\mathbf{H}(\mathbf{x})><\boldsymbol{\mathcal{S}}_i^*>\right)\right) - \mathcal{I}^*(\mathbf{p}_i^*) \end{cases} \tag{15}$$

with $\mathbf{H}(\mathbf{x})$ parameterised locally by the Lie algebra of $\mathbb{SL}(3)$, with $\mathbf{A}_i, i = 1...8$ generators of the algebra (further details are given in Appendix II):

$$\mathbf{H}(\mathbf{x}) = \exp\left(\sum_{i=1}^{8} x_i\mathbf{A}_i\right) \tag{16}$$

Surprisingly this parameterisation is not standard [31] even though it has the advantage of ensuring that at each iteration the homography belongs to $\mathbb{SL}(3)$ and that we use the minimal amount of parameters.

The current Jacobian, noted $\mathbf{J}(\mathbf{0})$, and the reference Jacobian, noted $\mathbf{J}(\mathbf{x}_0)$, can be written as the product of four Jacobians. The complete expressions can be found in [32] (similar to Appendix IV):

$$\mathbf{J}(\mathbf{0}) = \mathbf{J}_{\mathcal{I}}\mathbf{J}_{\Pi}\mathbf{J}_w\mathbf{J}_{\mathbf{Hx}}(\mathbf{0}) \tag{17}$$

$$\mathbf{J}(\mathbf{x}_0) = \mathbf{J}_{\mathcal{I}^*}\mathbf{J}_{\Pi}\mathbf{J}_w\mathbf{J}_{(\overline{\mathbf{H}}^{-1}\widehat{\mathbf{H}}\mathbf{Hx})}(\mathbf{x}_0) \tag{18}$$

Using Proposition 1 in Appendix III, we obtain the property:

$$\mathbf{J}_{(\overline{\mathbf{H}}^{-1}\widehat{\mathbf{H}}\mathbf{Hx})}(\mathbf{x}_0)\mathbf{x}_0 = \mathbf{J}_{\mathbf{Hx}}(\mathbf{0})\mathbf{x}_0 \tag{19}$$

The scalar exponential function can help gain an insight into this property.

$$\forall t, \exp(-t_0)\exp(t) = \exp(-t_0 + t) \tag{20}$$

By a change of variable, we obtain:

$$[\nabla_t \exp(-t_0 + t)]_{t=t_0} = [\nabla_t \exp(t)]_{t=0}$$

For the matrix exponential, the property (20) is not valid in general (non-commutativity), however the unknown value $\mathbf{x}_0$ defines a subgroup in which the property holds.

Thus, in equation 10, we can use $\mathbf{J}_{\mathbf{Hx}}(\mathbf{0})\mathbf{x}_0$ instead of $\mathbf{J}_{(\overline{\mathbf{H}}^{-1}\widehat{\mathbf{H}}\mathbf{Hx})}(\mathbf{x}_0)\mathbf{x}_0$ where $\mathbf{J}_{\mathbf{Hx}}(\mathbf{0})$ is a constant Jacobian matrix. The update $\mathbf{x}_0$ of the second-order minimization algorithm can be computed as follows:

$$\mathbf{x}_0 = -\left(\left(\frac{\mathbf{J}_{\mathcal{I}} + \mathbf{J}_{\mathcal{I}^*}}{2}\right)\mathbf{J}_{\Pi}\mathbf{J}_w\mathbf{J}_{\mathbf{Hx}}(\mathbf{0})\right)^{+}\mathbf{f}(\mathbf{0}) \tag{21}$$

The computational complexity is almost the same as for first-order algorithms as the reference Jacobian $\mathbf{J}_{\mathcal{I}^*}$ only needs to be calculated once.

Obtaining $\mathbf{J}_{\mathcal{I}^*}$ and $\mathbf{J}_{\mathcal{I}}$, that are the Jacobians taken in the images (for example using a Sobel filter), is a remarkable property. It indicates that we can take into account the non-linear properties of the sensor simply through the Jacobian of the projection function $\mathbf{J}_\Pi$ (this appears in the derivation of the Jacobians in Appendix IV).

D. Tracking multiple planes

When tracking multiple planes, we have the choice either to track the planes independently, or to constrain the same motion for each plane which is the object of this section.

From equation 2, we can parameterise a homography by a transformation $\mathbf{T} \in \mathbb{SE}(3)$ and a plane normal $\mathbf{n}_d \in \mathbb{R}^3$. With the Lie algebra parameterisation of $\mathbf{T}$:

$$\mathbf{H}(\mathbf{T}(\mathbf{x}), \mathbf{n}_d) = \mathbf{H}\left(\exp\left(\sum_{i=1}^{6} x_i \mathbf{A}_i\right), \mathbf{n}_d\right) \tag{22}$$

We can now reformulate the problem by parameterising each plane with the same transformation $\mathbf{T}$. To track the template j in the current image $\mathcal{I}$ is to find the transformation $\mathbf{H}(\overline{\mathbf{T}}, \overline{\mathbf{n}}_d^j)$ that warps the lifting of that region to the lifting of the reference template of $\mathcal{I}^*$:

$$\forall i, j, \;\; \mathcal{I}\left(\Pi\left(\mathbf{w}<\mathbf{H}(\overline{\mathbf{T}}, \overline{\mathbf{n}}_d^j)><\boldsymbol{\mathcal{S}}_{ij}^*>\right)\right) = \mathcal{I}^*(\mathbf{p}_{ij}^*) \tag{23}$$

In other words, knowing an approximation $\widehat{\mathbf{T}}$ of $\overline{\mathbf{T}}$ and $\widehat{\mathbf{n}}_d^j$ of $\overline{\mathbf{n}}_d^j$, the problem is to find the incremental transformation $\mathbf{T}(\mathbf{x})$ and $\mathbf{n}_d^j(\mathbf{x})$ that minimises the SSD over all the pixels and over the l planes ($\mathbf{x}$ contains the 6 transformation parameters and the $3 \times l$ parameters for the normals and depths):

$$\left\{\begin{array}{lcl} F(\mathbf{x}) & = & \frac{1}{2}\sum_{j=1}^{l}\sum_{i=1}^{q_j} \|\mathbf{f}_{ij}\|^2 \\ \mathbf{f}_{ij} & = & \mathcal{I}\left(\Pi\left(\mathbf{w}<\mathbf{H}(\mathbf{T}(\mathbf{x})\widehat{\mathbf{T}}, \widehat{\mathbf{n}}_d^j + \mathbf{n}_d^j(\mathbf{x}))><\boldsymbol{\mathcal{S}}_{ij}^*>\right)\right) \\ & & -\mathcal{I}^*(\mathbf{p}_{ij}^*) \end{array}\right. \tag{24}$$

The minimal number of parameters in equation 24 is in fact $6+3\times l-1$ because the first homography has only 8 degrees of freedom. However the extra degree of freedom empirically gave better results probably due to the better conditioning of the Jacobian (all the values for the normals have the same amplitude).

Similarly to the previous case, the Jacobians $\mathbf{J}(\mathbf{0})$ and $\mathbf{J}(\mathbf{x}_0)$, that correspond respectively to the current and the reference Jacobians, can be written as (see Appendix IV):

$$\mathbf{J}(\mathbf{0}) = \mathbf{J}_{\mathcal{I}}\, \mathbf{J}_\Pi \left[\mathbf{J}_{H_T}\mathbf{J}_T(\mathbf{0}) \quad \mathbf{J}_{H_n}\mathbf{J}_n(\mathbf{0})\right] \tag{25}$$

$$\mathbf{J}(\mathbf{x}_0) = \mathbf{J}_{\mathcal{I}^*}\, \mathbf{J}_\Pi \left[\mathbf{J}_{H_T^*}\mathbf{J}_{T^*}(\mathbf{x}_0) \quad \mathbf{J}_{H_n^*}\mathbf{J}_{n^*}(\mathbf{x}_0)\right] \tag{26}$$

with H_T the homography seen as a function of the transformation $\mathbf{T}$ and H_n the homography seen as a function of the plane normal $\mathbf{n}_d$.

Using proposition 1, $\mathbf{J}_{T^*}(\mathbf{x}_0)\mathbf{x}_0 = \mathbf{J}_T(\mathbf{0})\mathbf{x}_0$ and $\mathbf{J}_{n^*}(\mathbf{x}_0)\mathbf{x}_0 = \mathbf{J}_n(\mathbf{0})\mathbf{x}_0$. If we assume that $\widehat{\mathbf{T}} \approx \overline{\mathbf{T}}$ and $\widehat{\mathbf{n}} \approx \overline{\mathbf{n}}$, $\mathbf{J}_{H_T^*} \approx \mathbf{J}_{H_T}$ and $\mathbf{J}_{H_n^*} \approx \mathbf{J}_{H_n}$, the update $\mathbf{x}_0$ can be computed as follows:

$$\mathbf{x}_0 = -\left(\left(\frac{\mathbf{J}_{\mathcal{I}} + \mathbf{J}_{\mathcal{I}^*}}{2}\right)\mathbf{J}_\Pi \left[\mathbf{J}_{H_T}T(\mathbf{0}) \quad \mathbf{J}_{H_n}n(\mathbf{0})\right]\right)^+ \mathbf{f}(\mathbf{0}) \tag{27}$$

The inversion of this matrix can be done efficiently by exploiting its sparse structure as discussed more in detail in Appendix I.

E. Efficient ESM implementation and variants

In this section, we will detail how to improve the computational cost of the ESM and stay close to the second-order convergence rate.

Algorithm 1 details a basic iterative descent method for tracking a single plane. The computation is split between evaluation of the cost function and calculation of the descent direction.

Algorithm 1: ESM tracking method: basic algorithm for a single plane

Data: Current image $\mathcal{I}$ and reference image $\mathcal{I}^*$.
(ε, k_{max}) : thresholds, $\widehat{\mathbf{H}}$: initial estimate
Result: Local minimum $\overline{\mathbf{H}}$
Calculate $\mathbf{J}_{\mathcal{I}^*}$ (eg. Prewitt, Sobel). k := 0; **found** := false
while *(not* **found***) and* $(k++ < k_{max})$ **do**
  Calculate $\mathbf{J}_{\mathcal{I}}$. Calculate $\mathbf{J}_{esm}$ from equation (21).
  $\mathbf{x}_0 = -(\mathbf{J}_{esm}^\top \mathbf{J}_{esm})^{-1}\mathbf{J}_{esm}^\top \mathbf{f}(\mathbf{0})$
  $\widehat{\mathbf{H}} \leftarrow \widehat{\mathbf{H}} e^{A(\mathbf{x}_0)}$
  if $\|\mathbf{x}_0\| < \varepsilon$ **then**
    found := true
  end
end

Let q be the number of pixels of the template (several hundred or several thousand) and m the number of parameters. In [33], the authors detail the cost in terms of operations of the different steps when tracking. The pseudo-inversion and more specifically the product $\mathbf{J}_{esm}^\top \mathbf{J}_{esm}$ is the most expensive step and requires $o(m^2 q)$ operations. Calculating the cost function in comparison has a complexity of $o(mq)$.

The idea behind the inverse compositional algorithm is to reduce the complexity to $o(mq + m^3)$ by pre-calculating the pseudo-inverse $(\mathbf{J}_{inv}^\top \mathbf{J}_{inv})^{-1}\mathbf{J}_{inv}^\top$, with $\mathbf{J}_{inv}$ the *reference* Jacobian. We may note that changes in the cost function due for example to occlusion (including the template partly going out of the image) cannot be handled without needing to recalculate $\mathbf{J}_{inv}^+$. It also should not be used when estimating the motion directly *even* when the structure is known as the reference Jacobian then depends on a *combination* of the displacement and structure. Equation (41) shows the dependency of every element of the Jacobian on motion *and* structure. We simulate possible effects of using an incorrect constant Jacobian in Section IV-A.1.

Similarly to the inverse compositional, we can consider alternative increments reducing the complexity to $o(mq+m^3)$:

- α**ESM**:

$$\mathbf{x}_0 = -\frac{(\mathbf{g}^\top \mathbf{J}_{inv}^p \mathbf{g})}{\|\mathbf{J}_{esm}\mathbf{J}_{inv}^p \mathbf{g}\|^2}\mathbf{J}_{inv}^p \mathbf{g} \tag{28}$$

  with $\mathbf{g} = \mathbf{J}_{esm}^\top \mathbf{f}(\mathbf{0})$ and $\mathbf{J}_{inv}^p = (\mathbf{J}_{inv}^\top \mathbf{J}_{inv})^{-1}$. The corrective term was found in the following way:
  - $(-\mathbf{g})$ can be considered as a second-order steepest descent direction,

– we then look for the corrective term α that minimises the second-order approximation to the cost function:

$$\begin{aligned} F(-\alpha \mathbf{J}_{inv}^{p}\mathbf{g}) &= \frac{1}{2}\left\|\mathbf{f}(\mathbf{0}) - \alpha \mathbf{J}_{esm}\mathbf{J}_{inv}^{p}\mathbf{g}\right\|^2 \\ &= F(\mathbf{0}) - \alpha \mathbf{f}(\mathbf{0})^\top \mathbf{J}_{esm}\mathbf{J}_{inv}^{p}\mathbf{g} \\ &\quad -\frac{1}{2}\alpha^2 \left\|\mathbf{J}_{esm}\mathbf{J}_{inv}^{p}\mathbf{g}\right\|^2 \end{aligned}$$

by differentiation we obtain the optimal α and the desired expression.

- **iESM**:

$$\mathbf{x}_0 = -\frac{(\mathbf{g}^\top \mathbf{J}_{esm}^{p}\mathbf{g})}{\|\mathbf{J}_{esm}\mathbf{J}_{esm}^{p}\mathbf{g}\|^2}\mathbf{J}_{esm}^{p}\mathbf{g} \tag{29}$$

with $\mathbf{g} = \mathbf{J}_{esm}^{\top}\mathbf{f}(\mathbf{0})$ and $\mathbf{J}_{esm}^{p} = (\mathbf{J}_{esm}^{\top}\mathbf{J}_{esm})^{-1}$ calculated at the beginning of the iterations. This approach is valid for explicit structure and motion. It can be justified by saying that at the beginning, we have the best second-order estimate and that we then correct the Jacobian so that it stays valid at the optimum. It is not as satisfying as the previous methods as the Jacobian will *not* be correct at the optimum. However if it is sufficiently good, it will lead to the optimum anyway.

Reducing the computational cost of the iterations is only one side of the problem. Ideally we would also want to diminish the number of iterations. The ESM algorithm, as a second-order method, converges faster and more often than a first-order method.

In Section IV, the different algorithms will be compared with the effect of the approximations on the convergence.

F. Outlier rejection

Outlier rejection is an important part of visual tracking when dealing with sequences in uncontrolled environments. Specularities or occlusions are common sources of tracking failure.

A standard technique to improve least-square estimates is to use a robust cost function (M-estimators) such as Tukey or Huber (see [10] and Appendix in [26]). The underlying idea is that the errors should follow a given profile (eg. Gaussian distribution) and that all the points that do not verify the distribution are considered as outliers. Outliers are given lower weights so as to avoid influencing the results. Applying this technique directly as in [10] means we are considering each pixel as an independent value. However the error is generally spatially correlated. This observation was used in [34] to devise a robust approach to tracking. The idea is to split the image in blocks and calculate an error that takes into account the standard deviation of the initial block (errors are expected to be higher in texture rich regions). The authors use the following error for a block B_i:

$$\mathbf{e}_i = \frac{F(\mathbf{x})_{\mathbf{p}\in B_i}}{\sigma[\mathcal{I}^*(\mathbf{p})]_{\mathbf{p}\in B_i}} \tag{30}$$

They then order the errors and keep a pre-defined percentage of blocks. Choosing a pre-defined value is not satisfactory as when there are few outliers useful information will be discarded and if there is a lot of noise outliers will be kept. We propose to simply use robust statistics on the errors in each pixel weighted by the standard deviation of a rectangular region around the pixel. We found that this approach gave stable results over quite a wide range of rectangle sizes (5×5 to 15×15) and gave better results than the per-pixel method as we will see in the experimental section.

IV. Experimental validation

In this section, we will make a distinction between 2-D tracking using for example homography estimation (as described in Section III-C) to 3-D tracking where the camera motion and the plane normals are explicitly estimated (as described in Section III-D).

A. Simulation

1) Applying the inverse compositional to explicit motion estimation (3-D tracking): As explained previously, the reference Jacobian for multiple planes depends not only on the structure but also on the camera pose. Using the inverse compositional (**IC**) or hyperplane approximation (**HA**) algorithm with a constant Jacobian in this case can lead to poor results as the Jacobian can have arbitrarily big errors. Alas the **IC** has often been used to track in this situation. We will now simulate possible effects of using the **IC** and **HA** in this situation.

Our simulation setup consists of a sequence of 100 images without any added noise and with small inter-frame displacements. Figure 5 shows images 1,50 and 100 respectively of the simulated sequence. The correct plane normal and distance (ie. the structure) were given as input to the different algorithms. In the case of the **HA**, a linear relationship was learnt between the Lie representations of small random $\mathbb{SE}(3)$ transformations (generating a homography through the given correct normal) and the difference between the reference image and the warped image.

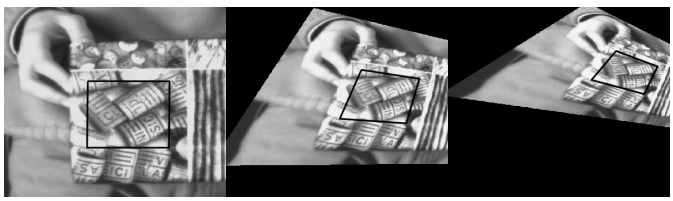

Fig. 5. Images 1, 50 and 100 of the simulated sequence

Figure 6 shows the number iterations taken to minimise and figure 7 the reprojection error after minimisation for each image of the sequence. As is evident from the graph, if the Jacobians are not recalculated, the **IC** and **HA** take more and more iterations. At the end of the sequence, the **IC** and **HA** took more than 500 iterations to converge. The **FC** took systematically 6 iterations and the **ESM** took 5 iterations at the same computational cost.

This experiment confirms that without recalculating the inverse compositional Jacobian (by explicit calculation or through learning) - which is the main advantage of using an inverse compositional formulation - **IC** and **HA** can lead to incorrect results for 3-D tracking *even* when the structure is

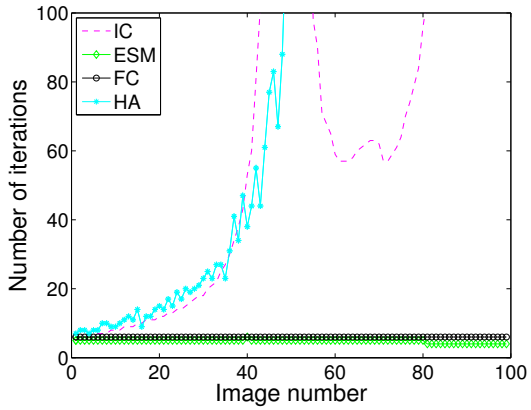

Fig. 6. Comparison of the number of iterations for the simulation sequence

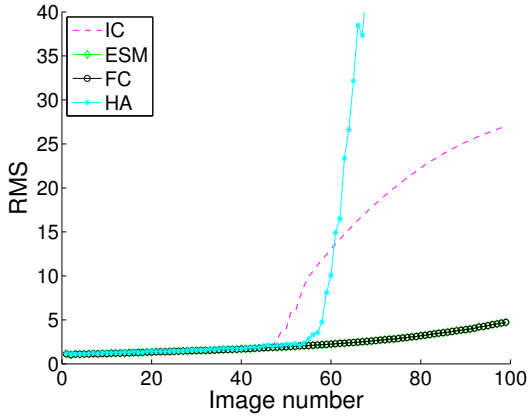

Fig. 7. Comparison of the reprojection error for the simulation sequence

known and the inter-frame displacement is small. This result is particularly important for omnidirectional visual tracking as we expect to track templates over larger image regions than for small field of view cameras.

These remarks do not apply of course to 2-D tracking (such as [25]) where the Jacobian is exactly constant (this comes from the subgroup property explained in Appendix III). In [19], the authors re-estimate the Jacobian for the 3-D tracking with **IC**, thus removing the advantage of this formulation of the problem. It is unclear if this is the case in [16].

2) Comparison between methods: The Matlab program written at the CMU for the project "Lucas-Kanade 20 Years On" was used to compare the convergence of the different algorithms[2].

The following methods were compared: forward compositional (**FC**) [10], inverse compositional (**IC**) [24], hyperplane approximation (**HA**) [25], efficient second-order minimisation (**ESM**), α**ESM** and **iESM** as described previously.

In the following, the **spatial noise** corresponds to a Gaussian reprojection error in the image of the corners of the tracked plane. The **image noise** is an independent and identically distributed Gaussian noise added to the image intensities (reference or warped image as specified by the context). The criterion chosen for the convergence of an algorithm is the root mean square (RMS) reprojection error of the image corners. An algorithm is said to have converged if the reprojection RMS of the plane corners is less than 1.

HA is different from the other algorithms in the sense that it requires a learning step to evaluate a matrix $\mathbf{J}^{\oplus}$ that plays the same role as the pseudo-inverse in (11). In this evaluation, we learnt $\mathbf{J}^{\oplus}$ for every 4 pixels in the image and applied 20 random motions for each pixels (in other words $20(100/4)^2 = 12500$ random homography transforms) with a spatial variance of 4 pixels. For $\mathbf{J}^{\oplus}$ to be valid in presence of noise, we also found it essential to learn in presence of noise. In this case, we learnt with a Gaussian random intensity noise added to the warped template of 6 pixels (the same amount of noise used for the evaluation). For a fair comparison, only every 4 pixels were used for *each* of the algorithms.

a) Evaluating the computational time per iteration: To evaluate the time taken for an iteration, we programmed the iteration steps in C language and tested the times for image sizes ranging from 20×20 to 500×500. The **IC** has the lowest computational cost and was compared to the other methods. In Fig. 8 we plot the iteration time versus the number of pixels. The ratios are reported in Table I. These results require comment. Why does the computational time increase *linearly* with the template size? Why is the difference between the **IC** and the other methods not greater?

The linear increase in computational time comes from the use of continuous blocks of memory that enables the instruction pointer (IP) to predict the next load by a constant stride calculation (here a "perfect" stride access pattern). The IP prefetcher then generates a prefetch request and loads the memory in the L1 cache (this property can be checked by making the same calculations but this time accessing the memory at random. The computational time is then no longer linear with template size).

The explanation concerning the computational time requires an explanation on the implementation to reduce memory access. A naive implementation would start by calculating $\mathbf{J}_{esm}$ (a matrix of size mp) and then $\mathbf{J}_{esm}^{+}\mathbf{f}(\mathbf{0})$ in two separate iterations. However it is not necessary to calculate $\mathbf{J}_{esm}$ explicitly. Instead it is possible to build $\mathbf{J}_{esm}^{\top}\mathbf{J}_{esm}$ (a symmetric matrix with $p(p-1)/2$ distinct values) and $\mathbf{J}_{esm}\mathbf{f}(\mathbf{0})$ (a vector of size p) in one loop over the image pixels with one access to the reference and current images and their gradients. The small amount of memory required for the computation ensures the values can be kept cached by the processor for read and write (and avoids the risk of random memory access). This aspect is rarely taken into account when calculating the computational cost of an algorithm: it can take longer to access memory than to recompute part of the data. The naive implementation leads to an algorithm that is about 3 times slower than the **IC** instead of only 1.8 in this one-pass approach.

We believe this aspect of computation should be taken into account when analysing the efficiency of computer vision algorithms as pre-calculating values (and thus making many memory accesses) can have the paradoxical effect of slowing down the algorithm. Only considering the number of operations can lead to incorrect conclusions.

[2]The Matlab source code can can be downloaded from `http://www.ri.cmu.edu/projects/project_515.html`

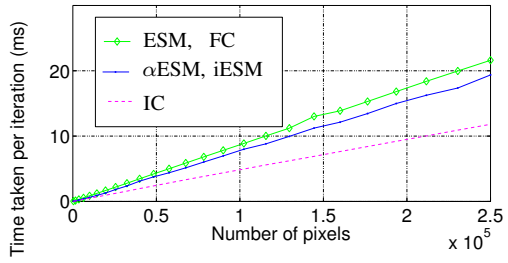

Fig. 8. Time (ms) vs number of pixels

TABLE I

ESTIMATED TIMES FOR AN ITERATION AND NUMBER OF ITERATIONS

	Time taken per iteration	Number of iterations given "at infinity"	Number of iterations given at "fixed time"
IC, HA	1	150	20
αESM, iESM	1.33	112	15
ESM, FC	1.8	83	11

b) Tests: The following tests were undertaken:

- "at infinity". Each algorithm is given a large amount of iterations (typically 150, see Table I). This is to test the convergence properties.
- "fixed time with added noise". an image noise of variance 6 was added to the warped image. This test simulates unmodeled errors that could appear through lighting changes or occlusion. We give a typical amount of iterations (eg. 20 for the **IC**, see Table I). The number of iterations are calculated in order to give the same amount of time to each algorithm.

Figures 9 and 10 show the frequency of convergence of the different algorithms as the homography transformation increases (the x-axis corresponds to the spatial error in pixels). The number of tests for each parameter variation was of 200 "at infinity" and 1000 in the other case.

The test "at infinity" confirms that there are two groups: the algorithms with a second-order convergence (**ESM** and variants) and the algorithms with first-order convergence properties. This experiment indicates that the **ESM** variants keep the second-order convergence rate despite the approximations. The **HA** has a good convergence rate for the range of spatial errors learnt but drops rapidly for stronger motion (and gives worse results than the **IC** or **FC** for very strong motion). The values during the learning phase were chosen to obtain a compromise between the rate of convergence and the robustness to noise. Learning stronger motions lead to a drop of the convergence rate for smaller motions.

The test at "fixed time with noise" shows that the two variants α**ESM** and **iESM** are possible alternatives to the direct **ESM** approach. The reason **iESM** has the same convergence rate as α**ESM** is that the calculation of the pseudo-inverse at the beginning of the iterations compensates in part for the image errors. Again **HA** provides a good convergence rate for small motions but this degrades with stronger motion.

3) Conclusion: In the simulation experiments we compared the convergence properties of the **ESM** algorithm and different

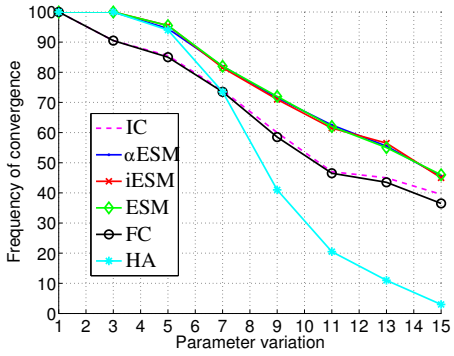

Fig. 9. Frequency of convergence vs homography motion for an "infinite time"

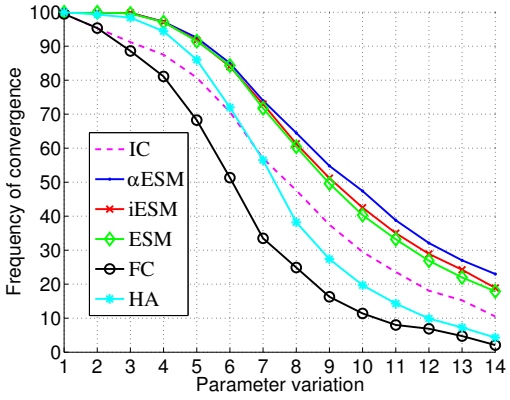

Fig. 10. Frequency of convergence vs homography motion for a "fixed time" with noise

variants to more standard approaches such as the inverse compositional (**IC**) and the forward compositional (**FC**). We showed that even though the iteration step of the **ESM** (and variants) is more computationally expensive than an iteration of the **IC**, the higher convergence rate makes it globally faster. If we add the possibility of working directly on occlusion (without having to calculate constant Jacobians by block such as in [34]), the algorithm is altogether a good alternative to the **IC** for image-based tracking. Variants of the **ESM**, α**ESM** and **iESM** were shown to improve the results further. An experiment also confirmed that the inverse compositional (**IC** and **HA**) with a constant Jacobian can lead to poor convergence for 3-D tracking even if the structure is known.

B. Real data

The algorithm was tested on real data obtained from a mobile robot. The central catadioptric camera was comprised of the S80 parabolic mirror from RemoteReality with a telecentric lens and perspective camera of resolution 1024×768 and calibrated using the open-source toolbox described in [27].

The experimental sequence consisted of 120 grey-level images taken with a fixed shutter speed and gain set to 0 over a distance of about 2 m. The sequence was taken so as to minimise slippage and enable to consider the robot odometry as ground truth. These experiments were undertaken

to analyse the precision of the algorithm for motion estimation. Another aspect that needed to be confirmed is the advantage of imposing the same camera motion when tracking different planes.

Figure 14(a) shows the templates chosen by hand and tracked in the experiment. The planes are numbered in counterclockwise order from 1 to 3 starting top left. To fix the scale factor, we measured the distance from the camera to plane 3 (0.5 m) (the plane that proved the stablest while tracking).

In the case of single plane tracking (**SPT**), for each homography, a translation $\mathbf{t}$ up to a scale factor and a rotation $\mathbf{R}$ was extracted (the ambiguity was solved by using several frames). The results show the median of the 3 extracted translations and rotations.

The algorithm for multiple plane tracking was tested with the **ESM** (**MPT ESM**), the **ESM** with a simple Huber robust approach (**MPT ESM HUB**) and the proposed approach for dealing with occlusion (**MPT ESM HUB BL**). The initial values given for the normals with depths was $[1;0;0]$ (the same results were obtained for values $[0;1;0]$, $[0;0;1]$, $[0;0;1000]$ ...). These initial values are far from the "real" values that can be deduced from Fig. 11 and 17 (with d_3=0.5 m): $[0.38;0.31;0]$, $[0.4;0.6;0]$ and $[1.2;1.6;0]$. The algorithm proved to be relatively insensitive to the initial values when an extra degree of freedom was given. This can be explained from the normals appearing in the homography as a product with the translation.

Figures 14(a) to 14(e) show the tracked regions during the sequence. Figures 15(a) to 16(d) show the errors obtained using the different methods on the left axis and the number of iterations needed to converge on the right axis with a dash-dot line (up to a maximum value of 40 iterations). The normals estimated on-line are represented in Fig. 17 and the distances estimated for planes 1 and 2 are detailed in Fig. 11 using the **MPT_ESM_HUB_BL** algorithm.

The first result that becomes clear is the improvement in terms of precision and robustness obtained by constraining the same motion for each tracked plane. As can be seen in Fig. 15(a) and 16(a) the patches did not have enough information to enable a good estimate of the motion. With a specularity appearing around image 70 on the stablest estimated plane, the motion estimation becomes erratic (Fig. 12). By imposing the same motion, the tracking algorithm does not fail even though the motion estimation still suffers from the non-robust minimisation approach (Fig. 15(b) and 16(b)). Applying the robust Huber cost function improves the precision and robustness (Fig. 15(c) and 16(c)) but greatly reduces the speed of convergence. What is not visible in the figure is that the normal estimates become incorrect towards the end of the sequence. The proposed approach (Fig. 12, 13, 15(d) and 16(d)) not only gives more precise results but also avoids very slow convergence.

The estimation of the plane distances are quite noisy (Fig. 11). In the first few iterations, this is easily explained by the small baseline. In the subsequent frames, the distance estimate oscillates within a range of about 20 cm for plane 1 and 10 cm for plane 2. Plane 1 does not benefit from an important baseline as can be seen from the trajectory in Fig. 12 and the 3-D reconstruction in Fig. 13 which explains why the distance estimate is quite unstable. Furthermore, fixing the distance of plane 3 increases the effect of noise that is propagated to the estimates of planes 1 and 2.

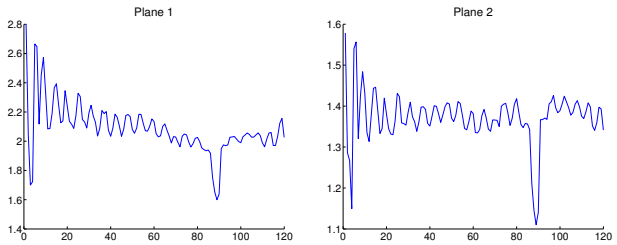

Fig. 11. Estimation of the plane distances for planes 1 and 2 with **MPT_ESM_HUB_BL** (m)

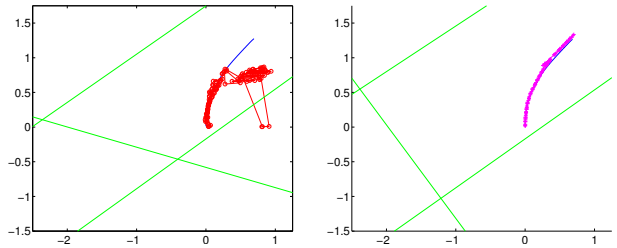

Fig. 12. Robot's motion in the XY-plane for **SPT** and **MPT_ESM_HUB_BL**

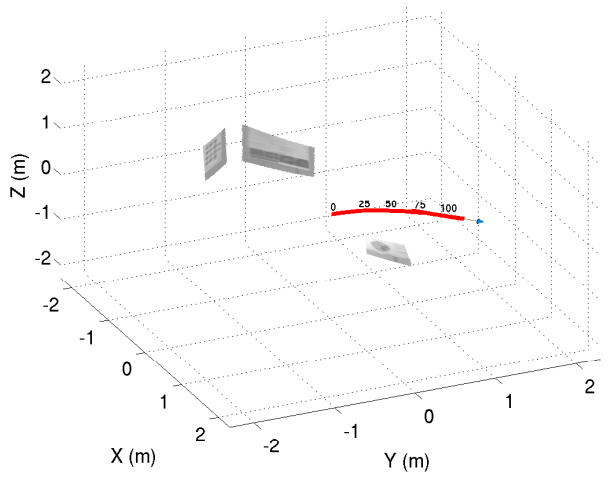

Fig. 13. Robot trajectory with 3-D reconstruction

V. Discussions and Conclusion

Large field of view sensors can improve structure from motion by enabling regions of the image to be tracked over longer periods. The aim of this article was to enable tracking with these type of sensors by taken into account the strong distortion induced by the non-linear projections. We also studied the problems of efficiency and proposed minimisation techniques (ESM and variants) adapted to real-time frameworks for image-based and 3-D structure and motion estimation. We

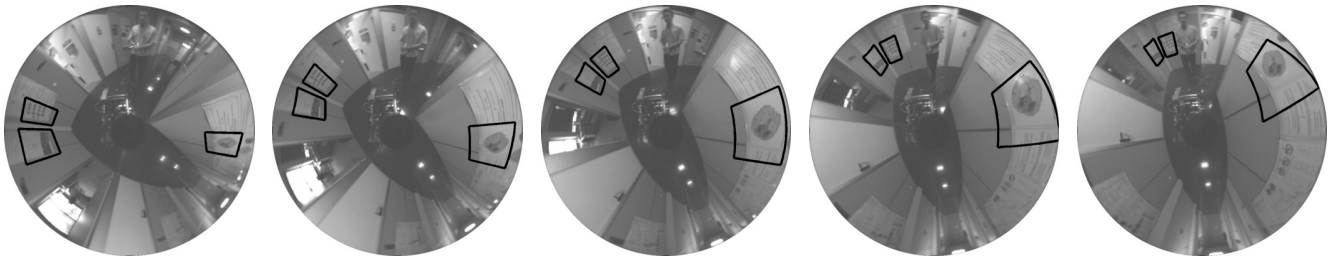

(a) Reference image (b) Image 30 (c) Image 60 (d) Image 90 (e) Image 120

Fig. 14. Tracked templates in the image sequence

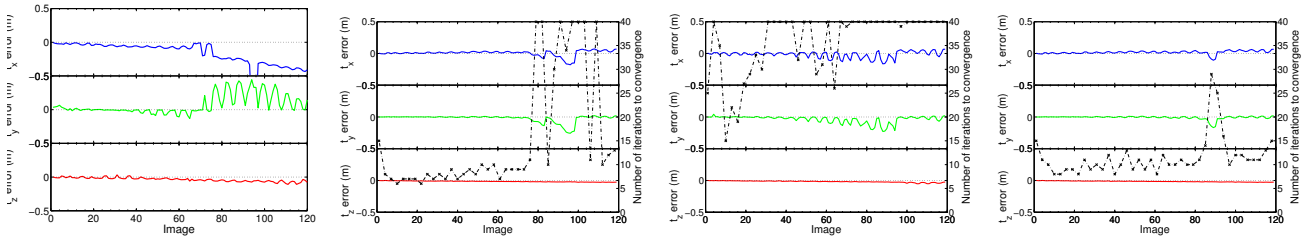

(a) Translation error with **SPT** (m) (b) Translation error with **MPT_ESM** (m) (c) Translation error with **MPT_ESM_HUB** (m) (d) Translation error with **MPT_ESM_HUB_BL** (m)

Fig. 15. Translation errors for the different algorithms

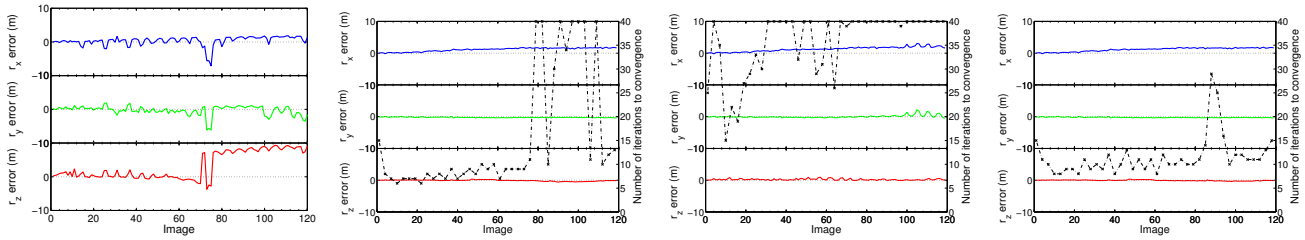

(a) Rotation error with **SPT** (deg) (b) Rotation error with **MPT_ESM** (deg) (c) Rotation error with **MPT_ESM_HUB** (deg) (d) Rotation error with **MPT_ESM_HUB_BL** (deg)

Fig. 16. Rotation errors for the different algorithms

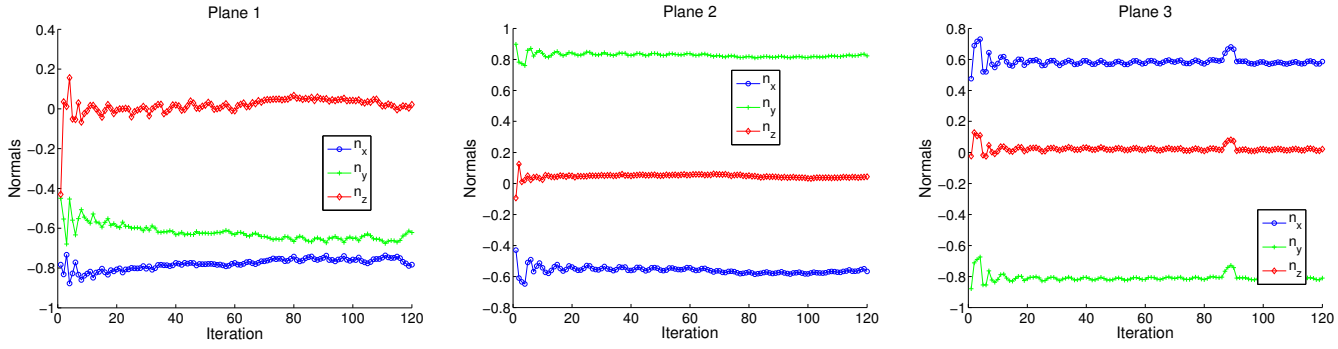

Fig. 17. Normals estimated for planes 1 to 3 with **MPT_ESM_HUB_BL**

showed that given a fixed time, the ESM algorithm has better convergence properties than the inverse compositional. Several variants to the ESM with better computational properties were also presented. A simple outlier rejection algorithm was proposed that takes into account the spatial correlation of the error and does not reduce the convergence rate as much as the per-pixel application of M-estimators. This work applied to the motion estimation of a mobile robot shows that it is a valid approach for robotic tasks such as visual servoing or simultaneous localisation and mapping.

APPENDIX I
EFFICIENT SOLVING OF THE NORMAL EQUATIONS

The Jacobian $\mathbf{J}$ appearing in the estimation of the pose between two views and the position of l planes (observed through q_j intensity values) has a sparse structure as in bundle adjustment [26] that can be used to solve efficiently the normal equations $\mathbf{J}\mathbf{x}_0 = -\mathbf{f}(\mathbf{0})$.

$\mathbf{J}$ has $r = \sum_{j=1}^{l} q_j$ rows for every pixel for every plane. $\mathbf{J}_{r\times(6+3l)} = [\mathbf{T}_{r\times 6}|\mathbf{P}_{r\times 3l}]$ with $\mathbf{T}$ a dense matrix representing the Jacobian with respect to the transformation for every plane and $\mathbf{P}$ a block-diagonal matrix with l blocks $\mathbf{N}_j$ of q_j rows and three columns representing the Jacobian with respect to the normals.

$$\mathbf{P}_{r\times 3l} = \begin{bmatrix} \mathbf{N}_{1\ q_1\times 3} & \mathbf{0}_{q_1\times 3} & \cdots & \mathbf{0}_{q_1\times 3} \\ \mathbf{0}_{q_2\times 3} & \mathbf{N}_{2\ q_2\times 3} & \cdots & \mathbf{0}_{q_2\times 3} \\ \vdots & \vdots & \ddots & \vdots \\ \mathbf{0}_{q_l\times 3} & \mathbf{0}_{q_2\times 3} & \cdots & \mathbf{N}_{l\ q_l\times 3} \end{bmatrix}$$

The normal equations can now be written as:

$$\mathbf{J}\mathbf{x}_0 = [\mathbf{T}_{r\times 6}|\mathbf{P}_{r\times 3l}] \begin{bmatrix} \mathbf{x}_T \\ \mathbf{x}_P \end{bmatrix} = -\mathbf{f}(\mathbf{0}) \tag{31}$$

This leads to the following form:

$$\begin{bmatrix} \mathbf{T}^\top\mathbf{T} & \mathbf{T}^\top\mathbf{P} \\ \mathbf{P}^\top\mathbf{T} & \mathbf{P}^\top\mathbf{P} \end{bmatrix} \begin{bmatrix} \mathbf{x}_T \\ \mathbf{x}_P \end{bmatrix} = - \begin{bmatrix} \mathbf{T}^\top\mathbf{f}(\mathbf{0}) \\ \mathbf{P}^\top\mathbf{f}(\mathbf{0}) \end{bmatrix} \tag{32}$$

multiplying on the left by $\begin{bmatrix} \mathbf{I}_{6\times 6} & -\mathbf{T}^\top\mathbf{P}(\mathbf{P}^\top\mathbf{P})^{-1} \\ \mathbf{0}_{3l\times 6} & \mathbf{I}_{3l\times 3l} \end{bmatrix}$, we eliminate the top right hand block:

$$\begin{aligned}(\mathbf{T}^\top\mathbf{T} - \mathbf{T}^\top\mathbf{P}(\mathbf{P}^\top\mathbf{P})^{-1}\mathbf{P}^\top\mathbf{T})\mathbf{x}_T = \\ -\mathbf{T}^\top\mathbf{f}(\mathbf{0}) + \mathbf{T}^\top\mathbf{P}(\mathbf{P}^\top\mathbf{P})^{-1}\mathbf{P}^\top\mathbf{f}(\mathbf{0})\end{aligned} \tag{33}$$

The key observation is that $\mathbf{P}^\top\mathbf{P}$ is block-diagonal with blocks of size 3×3 so the complexity of the inversion is linear with the number of planes. The calculation of $\mathbf{P}^\top\mathbf{P}$ is the limiting factors with a complexity in $O(3^2lq)$ (3 because of the 3 parameters encoding the normal) with q depending on the number of pixels per plane.

Solving (33) by the inversion of the left hand side (6×6 matrix), $\mathbf{x}_T$ can be obtained and used to find $\mathbf{x}_P$ by back-substitution (exploiting again the block-diagonal shape of $\mathbf{P}$):

$$\mathbf{x}_P = -(\mathbf{P}^\top\mathbf{P})^{-1}(\mathbf{P}^\top\mathbf{f}(\mathbf{0}) + \mathbf{P}^\top\mathbf{T}\mathbf{x}_T) \tag{34}$$

Written in this way, the computation of the normal equations is no longer in $O\left(\max[r(6+3l)^2, (6+3l)^3]\right)$ from the calculation or inversion of $\mathbf{J}^\top\mathbf{J}$ respectively but in $O(3^2lq)$ (linear in the number of planes).

APPENDIX II
LIE ALGEBRA PARAMETERISATION

A. Lie groups and Lie algebras

A Lie group is a group that locally has the topology of $\mathbb{R}^n$ everywhere (i.e. it is a smooth manifold). $\mathbb{SL}(3)$ (Special Linear Group) and $\mathbb{SE}(3)$ (Special Euclidean Group) that are of interest in this article are matrix Lie groups.

Let G be a matrix Lie group. The Lie algebra of G, denoted $\mathfrak{g}$ can be introduced as the set of all matrices $\mathbf{X}$ such that $e^{t\mathbf{X}}$ (exponential map) is in G for all real numbers t.

An element of $g \in G$ can be expressed in terms of n independent elements of G with n the dimension of the group ($n = 8$ for $\mathbb{SL}(3)$ and $n = 6$ for $\mathbb{SE}(3)$).

If g only depends on a parameter t_i:

$$g(t_i) = \exp(t_i\mathbf{A}_i), \text{by differentiating} : \mathbf{A}_i = \left.\frac{\partial g(t_i)}{\partial t_i}\right|_{t_i=0}$$

$\mathbf{A}_i$ is referred to as a generator of the Lie algebra and is independent of t. If the group is connected, $\mathbf{A}_i$ can form a path to any the matrix of the form of g starting from the identity. If we repeat the operation of differentiation around the identity for each independent element of the group, we obtain the set of all generators of the Lie algebra.

B. Lie algebras for optimisation

With G a matrix Lie group of dimension n, let:

$$\begin{array}{rccc} f: & G & \longrightarrow & \mathbb{R} \\ & \mathbf{g} & \longmapsto & f(\mathbf{g}) \end{array}$$

In this article, g corresponds to a homography $\mathbf{H}$ for $G = \mathbb{SL}(3)$ or a transformation $\mathbf{T}$ for $G = \mathbb{SE}(3)$.

Consider the following minimisation problem, with d a differentiable distance and $\overline{\mathbf{f}} \in \mathbb{R}$:

$$\overline{\mathbf{g}} = \min_{\mathbf{g}}\ d(f(\mathbf{g}), \overline{\mathbf{f}})$$

When applying gradient descent to find a minimum, we start from an initial value $\widehat{\mathbf{g}}$ and at each step add a value $\mathbf{g}_k$ calculated typically from the Jacobian: $\widehat{\mathbf{g}} \leftarrow \widehat{\mathbf{g}} + \mathbf{g}_k$. As such, there is no guarantee that the new value of $\widehat{\mathbf{g}}$ will belong to the group G. To solve this problem, the new $\widehat{\mathbf{g}}$ is often projected onto the group manifold but this can alter the convergence speed and the region of convergence.

Alternatively, we can define a new function h. With $\mathfrak{g}$ the Lie algebra of G and $\times$ the group operation:

$$\begin{array}{rccccc} h: & \mathbb{R}^n & \longrightarrow & \mathfrak{g} & \longrightarrow & \mathbb{R} \\ & \mathbf{x} & \longmapsto & G(\mathbf{x}) & \longmapsto & f(\widehat{\mathbf{g}} \times e^{G(\mathbf{x})}) \end{array}$$

h is only defined *locally* by the Lie algebra parameterisation of G. If we apply a gradient descent approach to h, we will start at $\mathbf{x} = 0$ (that corresponds to the initial value of f) and the update will be written: $\widehat{\mathbf{g}} \leftarrow \widehat{\mathbf{g}} \times e^{G(\mathbf{x}_k)}$. We are now sure that at each step, the new value of $\widehat{\mathbf{g}}$ belongs to the Lie group G. In this article, the update operations are $\widehat{\mathbf{H}} \leftarrow \widehat{\mathbf{H}}\mathbf{H}(\mathbf{x}_k)$ and $\widehat{\mathbf{T}} \leftarrow \mathbf{T}(\mathbf{x}_k)\widehat{\mathbf{T}}$ for $\mathbb{SL}(3)$ and $\mathbb{SE}(3)$ respectively.

To be able to link $\widehat{\mathbf{g}}$ to $\overline{\mathbf{g}}$ by infinitesimal transformation, we must make sure that the values are path-connected (i.e. belong to the same component). This will always be the case for $\mathbb{SL}(3)$ and $\mathbb{SE}(3)$ as these groups have a single component.

APPENDIX III
PROOF OF THE LIE SUB-GROUP PROPERTY

Proposition 1: Let G be a matrix Lie group of dimension n and $\mathbf{A}(\mathbf{x})$ be an $n \times n$ real matrix belonging to the associated Lie algebra and seen as a function of $\mathbf{x} \in \mathbb{R}^n$:

$$\forall \mathbf{x}_0 \in \mathbb{R}^n,\ \left.\frac{d(e^{-\mathbf{A}(\mathbf{x}_0)}e^{\mathbf{A}(\mathbf{x})})}{d\mathbf{x}}\right|_{\mathbf{x}=\mathbf{x}_0} \mathbf{x}_0 = \left.\frac{de^{\mathbf{A}(\mathbf{x})}}{d\mathbf{x}}\right|_{\mathbf{x}=\mathbf{0}} \mathbf{x}_0 \quad (35)$$

Proof: (This proof is valid for any Lie group even with an implicit representation.) Let g be a function of $\mathbb{R}^n$ with the property $g((1+t)\mathbf{x}_0) = g(\mathbf{x}_0)g(t\mathbf{x}_0)$ (property of the subgroup defined by $\mathbf{x}_0$). In the statement, $g(t\mathbf{x}) = e^{t\mathbf{A}(\mathbf{x})}$.

By differentiating the two expressions:

$$\left.\frac{dg((1+t)\mathbf{x}_0)}{dt}\right|_{t=0} = \left.\frac{dg(\mathbf{x})}{d\mathbf{x}}\right|_{\mathbf{x}=\mathbf{x}_0} \mathbf{x}_0 \quad (36)$$

$$\left.\frac{dg(\mathbf{x}_0)g(t\mathbf{x}_0)}{dt}\right|_{t=0} = g(\mathbf{x}_0)\left.\frac{dg(\mathbf{x})}{d\mathbf{x}}\right|_{\mathbf{x}=0} \mathbf{x}_0 \quad (37)$$

Multiplying each equation by $g(\mathbf{x}_0)^{-1}$ and with the property $g(\mathbf{x}_0)^{-1} = g(-\mathbf{x}_0)$ (group property), (35) is obtained. ■

APPENDIX IV
JACOBIAN FOR TRACKING MULTIPLE PLANES

The translation can only be obtained up to a scale factor so to avoid over-parameterising the system, the "first plane" can be estimated differently:

$$\mathbf{H}_1 = \mathbf{R} + \frac{\mathbf{t}}{d_1}\mathbf{n}_1^\top,\ \ \mathbf{H}_i = \mathbf{R} + \frac{\mathbf{t}}{d_1}\left(\frac{d_1}{d_i}\mathbf{n}_i^\top\right),\ \ (i>1) \quad (38)$$

In other words, we can only estimate two parameters for $\mathbf{n}_1$ (for example by normalising) and three for $\frac{d_1}{d_i}\mathbf{n}_i$, $i > 1$.

For clarity, we will no longer indicate i, j and d.

A. Current Jacobian

The current Jacobian can be written (dropping $\mathcal{I}^*(\mathbf{p}^*)$):

$$\begin{aligned}\mathbf{J}(\mathbf{0}) &= \left[\nabla_{\mathbf{x}}\, \mathcal{I}\left(\Pi(\mathbf{w}<\mathbf{H}(\mathbf{T}(\mathbf{x})\widehat{\mathbf{T}}, \widehat{\mathbf{n}} + \mathbf{n}(\mathbf{x}))><\boldsymbol{\mathcal{S}}^*>)\right)\right]_{\mathbf{x}=\mathbf{0}} \\ &= \mathbf{J}_{\mathcal{I}}\mathbf{J}_{\Pi}\,\mathbf{J}_w[\mathbf{J}_{H_T T}(\mathbf{0})\ \ \mathbf{J}_{H_n n}(\mathbf{0})]\end{aligned}$$

The group properties of $\mathbf{w}$ imply:

$$\mathbf{w}<\mathbf{H}(\mathbf{T}(\mathbf{x})\widehat{\mathbf{T}}, \widehat{\mathbf{n}}+\mathbf{n}(\mathbf{x}))><\boldsymbol{\mathcal{S}}^*> = \mathbf{w}<\mathbf{H}(\widehat{\mathbf{T}}, \widehat{\mathbf{n}})><\Pi^{-1}(\mathbf{q})>$$

with: $\mathbf{q} = \Pi(\mathbf{w}<\mathbf{H}(\widehat{\mathbf{T}}, \widehat{\mathbf{n}})^{-1}\mathbf{H}(\mathbf{T}(\mathbf{x})\widehat{\mathbf{T}}, \widehat{\mathbf{n}} + \mathbf{n}(\mathbf{x}))><\boldsymbol{\mathcal{S}}^*>)$
In $\mathbf{0}$, $\mathbf{q} = \Pi(\mathbf{w}<\mathbf{I}><\boldsymbol{\mathcal{S}}^*>)$ so the first Jacobian $\mathbf{J}_{\mathcal{I}}$ is:

$$\mathbf{J}_{\mathcal{I}} = \left[\nabla_{\mathbf{q}}\, \mathcal{I}\left(\Pi(\mathbf{w}<\mathbf{H}(\widehat{\mathbf{T}}, \widehat{\mathbf{n}})><\Pi^{-1}(\mathbf{q})>)\right)\right]_{\mathbf{q}=\mathbf{p}}$$

The pixels coordinates are transformed according to the current motion and normal estimates, $\mathbf{J}_{\mathcal{I}}$ is thus the Jacobian of the warped current image.

$\mathbf{J}_\Pi$ and $\mathbf{J}_w$ are constant Jacobians.

$$\mathbf{J}_{H_T} = \left[\nabla_{\mathbf{T}}\, \mathbf{H}(\widehat{\mathbf{T}}, \widehat{\mathbf{n}})^{-1}\mathbf{H}(\mathbf{T}\widehat{\mathbf{T}}, \widehat{\mathbf{n}})\right]_{\mathbf{T}=\mathbf{I}} \quad (39)$$

$$\mathbf{J}_T(\mathbf{0}) = [\nabla_{\mathbf{x}}\, \mathbf{T}(\mathbf{x})]_{\mathbf{x}=\mathbf{0}} \quad (40)$$

Let $\widehat{\mathbf{T}} = \begin{bmatrix} \widehat{\mathbf{R}} & \widehat{\mathbf{t}} \\ \mathbf{0} & 1 \end{bmatrix}$ and $\widehat{\boldsymbol{\tau}} = (\widehat{\tau}_x, \widehat{\tau}_y, \widehat{\tau}_z) = \frac{-\widehat{\mathbf{R}}^\top\widehat{\mathbf{t}}}{1+\widehat{\mathbf{n}}^\top\widehat{\mathbf{R}}^\top\widehat{\mathbf{t}}}$.

We also define $\mathbf{e}_1 = [1\ 0\ 0]^\top$, $\mathbf{e}_2 = [0\ 1\ 0]^\top$ and $\mathbf{e}_3 = [0\ 0\ 1]^\top$ (canonical vectors).

If we write $\mathbf{J}_{H_T T} = \mathbf{J}_{H_T}\mathbf{J}_T$ it can be shown by algebraic manipulation that:

$$\mathbf{J}_{H_T T} = \begin{bmatrix} \widehat{\mathbf{n}}\,(\widehat{\tau}_x\widehat{\mathbf{n}} + \mathbf{e}_1)^\top\widehat{\mathbf{R}}^\top & \widehat{\mathbf{H}}^\top[\widehat{\tau}_x\widehat{\mathbf{n}} + \mathbf{e}_1]_\times\mathbf{I} \\ \widehat{\mathbf{n}}\,(\widehat{\tau}_y\widehat{\mathbf{n}} + \mathbf{e}_2)^\top\widehat{\mathbf{R}}^\top & \widehat{\mathbf{H}}^\top[\widehat{\tau}_y\widehat{\mathbf{n}} + \mathbf{e}_2]_\times\mathbf{I} \\ \widehat{\mathbf{n}}\,(\widehat{\tau}_z\widehat{\mathbf{n}} + \mathbf{e}_3)^\top\widehat{\mathbf{R}}^\top & \widehat{\mathbf{H}}^\top[\widehat{\tau}_z\widehat{\mathbf{n}} + \mathbf{e}_3]_\times\mathbf{I} \end{bmatrix} \quad (41)$$

$$\mathbf{J}_{H_n} = \left[\nabla_{\mathbf{n}}\, \mathbf{H}(\widehat{\mathbf{T}}, \widehat{\mathbf{n}})^{-1}\mathbf{H}(\widehat{\mathbf{T}}, \mathbf{n})\right]_{\mathbf{n}=\widehat{\mathbf{n}}} \quad (42)$$

$$\mathbf{J}_n(\mathbf{0}) = [\nabla_{\mathbf{x}}\, \widehat{\mathbf{n}} + \mathbf{n}(\mathbf{x})]_{\mathbf{x}=\mathbf{0}} = \mathbf{I} \quad (43)$$

$$\mathbf{J}_{H_n n} = \mathbf{J}_{H_n}\mathbf{J}_n(\mathbf{0}) = \begin{bmatrix} (\widehat{\tau}_x\widehat{\mathbf{n}} + \mathbf{e}_1)^\top\widehat{\mathbf{R}}^\top\widehat{\mathbf{t}}\mathbf{J}_i \\ (\widehat{\tau}_y\widehat{\mathbf{n}} + \mathbf{e}_2)^\top\widehat{\mathbf{R}}^\top\widehat{\mathbf{t}}\mathbf{J}_i \\ (\widehat{\tau}_z\widehat{\mathbf{n}} + \mathbf{e}_3)^\top\widehat{\mathbf{R}}^\top\widehat{\mathbf{t}}\mathbf{J}_i \end{bmatrix} \quad (44)$$

with $\mathbf{J}_i = \left[\nabla_{\mathbf{n}}\ \frac{\widehat{\mathbf{n}}+\mathbf{n}}{\|\widehat{\mathbf{n}}+\mathbf{n}\|}\right]_{\mathbf{n}=\mathbf{0}}$ if $i = 1$ and $\mathbf{J}_i = \mathbf{I}_3$ for $i > 1$ (to take into account the normalisation of $\mathbf{n}_1$).

B. Reference Jacobian

The reference Jacobian can be written (dropping $\mathcal{I}^*(\mathbf{p}^*)$):

$$\begin{aligned}\mathbf{J}(\mathbf{x}_0) &= \left[\nabla_{\mathbf{x}}\mathcal{I}\left(\Pi(\mathbf{w}<\mathbf{H}(\mathbf{T}(\mathbf{x})\widehat{\mathbf{T}}, \widehat{\mathbf{n}}+\mathbf{n}(\mathbf{x}))><\boldsymbol{\mathcal{S}}^*>)\right)\right]_{\mathbf{x}=\mathbf{x}_0} \\ &= \mathbf{J}_{\mathcal{I}^*}\,\mathbf{J}_\Pi\,\mathbf{J}_w\,[\mathbf{J}_{H_T^* T^*}(\mathbf{x}_0)\ \ \mathbf{J}_{H_n^* n^*}(\mathbf{x}_0)]\end{aligned}$$

The group properties of $\mathbf{w}$ imply:

$$\mathbf{w}<\mathbf{H}(\mathbf{T}(\mathbf{x})\widehat{\mathbf{T}}, \widehat{\mathbf{n}}+\mathbf{n}(\mathbf{x}))><\boldsymbol{\mathcal{S}}^*> = \mathbf{w}<\mathbf{H}(\overline{\mathbf{T}}, \overline{\mathbf{n}})><\Pi^{-1}(\mathbf{q})>$$

with: $\mathbf{q} = \Pi(\mathbf{w}<\mathbf{H}(\overline{\mathbf{T}}, \overline{\mathbf{n}})^{-1}\mathbf{H}(\mathbf{T}(\mathbf{x})\widehat{\mathbf{T}}, \widehat{\mathbf{n}} + \mathbf{n}(\mathbf{x}))><\boldsymbol{\mathcal{S}}^*>)$
In $\mathbf{x}_0$, $\mathbf{q} = \Pi(\mathbf{w}<\mathbf{I}><\boldsymbol{\mathcal{S}}^*>)$ so the first Jacobian $\mathbf{J}_{\mathcal{I}^*}$ is:

$$\begin{aligned}\mathbf{J}_{\mathcal{I}^*} &= \left[\nabla_{\mathbf{q}}\, \mathcal{I}\left(\Pi(\mathbf{w}<\mathbf{H}(\overline{\mathbf{T}}, \overline{\mathbf{n}})><\Pi^{-1}(\mathbf{q})>)\right)\right]_{\mathbf{q}=\mathbf{p}} \\ &= [\nabla_{\mathbf{q}}\, \mathcal{I}^*(\mathbf{q})]_{\mathbf{q}=\mathbf{p}} \quad (45)\end{aligned}$$

This Jacobian is taken after applying the optimal transformation which transforms the pixel coordinates to the exact locations in the current image that correspond to the same image intensities as the reference template by hypothesis. Thus this expression is the Jacobian of the reference image.

$$\mathbf{J}_{H_T^*} = \left[\nabla_{\mathbf{T}}\, \mathbf{H}(\overline{\mathbf{T}}, \overline{\mathbf{n}})^{-1}\mathbf{H}(\mathbf{T}\overline{\mathbf{T}}, \widehat{\mathbf{n}})\right]_{\mathbf{T}=\mathbf{I}} \quad (46)$$

$$\mathbf{J}_{T^*}(\mathbf{x}_0) = \left[\nabla_{\mathbf{x}}\, \mathbf{T}(\mathbf{x})\widehat{\mathbf{T}}\overline{\mathbf{T}}^{-1}\right]_{\mathbf{x}=\mathbf{x}_0} \quad (47)$$

$$\mathbf{J}_{H_n^*} = \left[\nabla_{\mathbf{T}}\, \mathbf{H}(\overline{\mathbf{T}}, \overline{\mathbf{n}})^{-1}\mathbf{H}(\widehat{\mathbf{T}}, \mathbf{n})\right]_{\mathbf{n}=\widehat{\mathbf{n}}} \quad (48)$$

$$\mathbf{J}_{n^*}(\mathbf{x}_0) = [\nabla_{\mathbf{x}}\, \widehat{\mathbf{n}} + \mathbf{n}(\mathbf{x})]_{\mathbf{x}=\mathbf{x}_0} = \mathbf{I} = \mathbf{J}_n(\mathbf{0}) \quad (49)$$

Trivially we have $\mathbf{J}_n(\mathbf{0})\mathbf{x}_0 = \mathbf{J}_{n^*}(\mathbf{x}_0)\mathbf{x}_0$ but also, thanks (35), $\mathbf{J}_{T^*}(\mathbf{x}_0)\mathbf{x}_0 = \mathbf{J}_T(\mathbf{0})\mathbf{x}_0$. Assuming $\widehat{\mathbf{T}} \approx \overline{\mathbf{T}}$ and $\widehat{\mathbf{n}} \approx \overline{\mathbf{n}}$, $\mathbf{J}_{H_T^*} \approx \mathbf{J}_{H_T}$ and $\mathbf{J}_{H_n^*} \approx \mathbf{J}_{H_n}$, we obtain equation (27).

REFERENCES

[1] Y. Yagi, "Omnidirectional sensing and its applications," *IEICE Trans, on Information and Systems*, vol. E82-D, no. 3, pp. 568–579, 1999.

[2] T.Pajdla, T.Svoboda, and V.Hlavac, *In Panoramic Vision: Sensors, Theory, and Applications*. Springer Verlag, 2001, ch. Epipolar Geometry of Central Panoramic Cameras, pp. 85–114.

[3] C. Geyer and K. Daniilidis, "Mirrors in motion: Epipolar geometry and motion estimation," in *International Conference on Computer Vision*, 2003.

[4] J. Barreto, F. Martin, and R. Horaud, "Visual servoing/tracking using central catadioptric cameras," in *International Symposium on Experimental Robotics*, ser. Advanced Robotics Series, 2002.

[5] H. Hadj-Abdelkader, Y. Mezouar, N. Andreff, and P. Martinet, "2 1/2 d visual servoing with central catadioptric cameras," in *IEEE International Conference on Intelligent Robots and Systems*, 2005.
[6] G. Silveira, E. Malis, and P. Rives, "An efficient direct method for improving visual slam," in *IEEE International Conference on Robotics and Automation*, 2007.
[7] A. I. Comport, E. Malis, and P. Rives, "Accurate quadrifocal tracking for robust 3d visual odometry," in *IEEE International Conference on Robotics and Automation*, 2007.
[8] B. D. Lucas and T. Kanade, "An iterative image registration technique with an application to stereo vision," *International Joint Conference on Artificial Intelligence*, pp. 674–679, 1981.
[9] J. Shi and C. Tomasi, "Good features to track," in *IEEE Conference on Computer Vision and Pattern Recognition*, 1994.
[10] G. D. Hager and P. N. Belhumeur, "Efficient region tracking with parametric models of geometry and illumination," *IEEE Transactions on Pattern Analysis and Machine Intelligence*, vol. 20, no. 10, pp. 1025–1039, 1998.
[11] H. Y. Shum and R. Szeliski, "Construction of panoramic image mosaics with global and local alignment," *International Journal on Computer Vision*, vol. 16, no. 1, pp. 63–84, 2000.
[12] S. Baker and I. Matthews, "Equivalence and efficiency of image alignment algorithms," in *IEEE Conference on Computer Vision and Pattern Recognition*, 2001, pp. 1090–1097.
[13] J. M. Buenaposada and L. Baumela, "Real-time tracking and estimation of planar pose," in *ICPR*, 2002, pp. 697–700.
[14] S. Benhimane and E. Malis, "Real-time image-based tracking of planes using efficient second-order minimization," in *IEEE International Conference on Intelligent Robots and Systems*, 2004.
[15] ——, "A new approach to vision-based robot control with omnidirectional cameras," in *IEEE International Conference on Robotics and Automation*, 2006.
[16] D. Cobzas and P. Sturm, "3d ssd tracking with estimated 3d planes," in *Proceedings of the Second Canadian Conference on Computer and Robot Vision, Victoria, Canada*, may 2005.
[17] S. Benhimane and E. Malis, "Homography-based 2d visual tracking and servoing," *International Journal of Robotic Research*, 2007.
[18] H. Jin, P. Favaro, and S. Soatto, "A semi-direct approach to structure from motion," *The Visual Computer*, vol. 19, no. 6, pp. 377–394, 2003.
[19] N. Molton, A. Davison, and I. Reid, "Locally planar patch features for real-time structure from motion," in *British Machine Vision Conference*, 2004.
[20] A. Bartoli, "A random samping strategy for piecewise planar scene segmentation," *Computer Vision and Image Understanding*, vol. 105, no. 1, pp. 42–59, 2007.
[21] G. Silveira, E. Malis, and P. Rives, "Real-time robust detection of planar regions in a pair of images," in *IEEE/RSJ International Conference on Intelligent Robots and Systems*, 2006.
[22] M. Cummins and P. Newman, "Probabilistic appearance based navigation and loop closing," in *IEEE International Conference on Robotics and Automation*, 2007.
[23] G. K. B. Williams and I. Reid, "Real-time slam relocalisation," in *International Conference on Computer Vision*, 2007.
[24] S. Baker, R. Patil, K. Cheung, and I. Matthews, "Lucas-kanade 20 years on: Part 5," Carnegie Mellon Robotics Institute, Tech. Rep., 2004.
[25] F. Jurie and M. Dhome, "Hyperplane approximation for template matching," *IEEE Transaction on Pattern Analysis and Machine Intelligence*, vol. 24, no. 7, pp. 996–1000, 2002.
[26] R. Hartley and A. Zisserman, *Multiple View geometry in Computer vision*. Cambridge university press, 2000.
[27] C. Mei and P. Rives, "Single view point omnidirectional camera calibration from planar grids," in *IEEE International Conference on Robotics and Automation*, April 2007.
[28] C. Geyer and K. Daniilidis, "Catadioptric projective geometry," *International Journal of Computer Vision*, vol. 45, no. 3, pp. 223–243, 2001.
[29] J. P. Barreto and H. Araujo, "Geometric properties of central catadioptric line images and their application in calibration," *IEEE Transactions on Pattern Analysis and Machine Intelligence*, vol. 27, no. 8, pp. 1327–1333, 2005.
[30] E. Malis, "Improving vision-based control using efficient second-order minimization techniques," in *IEEE International Conference on Robotics and Automation*, 2004.
[31] S. Baker, A. Datta, and T. Kanade, "Parameterizing homographies," Carnegie Mellon Robotics Institute, Tech. Rep., March 2006.
[32] C. Mei, S. Benhimane, E. Malis, and P. Rives, "Homography-based tracking for central catadioptric cameras," in *IEEE International Conference on Intelligent Robots and Systems*, October 2006.
[33] S. Baker, R. Patil, K. Cheung, and I. Matthews, "Lucas-kanade 20 years on: Part 1," Carnegie Mellon Robotics Institute, Tech. Rep., 2004.
[34] T. Ishikawa, I. Matthews, and S. Baker, "Efficient image alignment with outlier rejection," Carnegie Mellon Robotics Institute, Tech. Rep., 2002.

Christopher Mei graduated from the Institut d'Informatique d'Entreprise in Evry, near Paris, in 2003 and obtained an MS degree in Artificial Intelligence and Pattern Recognition from Paris VI in the same year. He undertook his PhD research at INRIA, Sophia Antipolis with the ICARE/ARobAS project team from 2003 to 2006. Since the beginning of 2007, he has been a research assistant at the University of Oxford in the Active Vision Group. His research interests include SLAM, visual tracking and omnidirectional vision.

Selim Benhimane obtained the Postgraduate degree of Engineering systems, Automation and Vision from the National School of Higher Education in Physics, Strasbourg, France in 2002. In the same year, he received a postgraduate advanced diploma in Photonics, Imaging and Cybernetics from Louis Pasteur University, Strasbourg, France. Then, he prepared his doctor thesis within the ICARE team at INRIA Sophia Antipolis and obtained his Ph.D. from the École Nationale Supérieure des Mines de Paris, France. Since 2005, he is a Research Associate in the Technical University of Munich, Germany. His research interests include computer vision, robotics, vision-based control. In November 2007, Selim Benhimane received from the Federation of Science and Information Technology Associations the prize of the Best French Doctor Thesis of the years 2005 and 2006 in the category Applied and Innovative Research.

Ezio Malis was born in Gorizia, Italy, in 1970 and graduated both from the University Politecnico di Milano and from the Ecole Supérieure d'Electricité (Suplec), Paris, in 1995. After a three years joint research work with IRISA/INRIA Rennes and with the national French company of electricity power (EDF), he received the Ph.D degree from the University of Rennes in 1998. He spent two years as research associate at the University of Cambridge (UK). He joined INRIA Sophia-Antipolis in 2000 as research scientist. His research interests include automatics, robotics, computer vision, and in particular vision-based control.

Patrick Rives Patrick Rives (M'04) received the PhD in robotics from the Universit des Sciences et Techniques du Languedoc, Montpellier, France, in 1981 and the Habilitation à Diriger les Recherches degree in 1991. He was a Research Fellow with the Institut National de la Recherche Scientifique (INRS) Laboratory, Montreal, QC, Canada, for one year. In 1982, he joined the Institut National de recherche en Informatique et Automatique (INRIA), Rennes, France. He is currently Research Director at INRIA Sophia Antipolis-Méditérranée at the head of the project-team ARobAS (Advanced Robotics and Autonomous Systems). His main research interests include mobile robot navigation, SLAM, visual servoing, sensing and scene modeling and sensor-based control. His main application fields are aerial and underwater robotics and intelligent urban vehicles.